



Controllable Phononic Low-Pass Filter via Optomechanical Interactions

Cheng Yang¹, Jiteng Sheng^{1,2,3*} and Haibin Wu^{1,2,4}

¹State Key Laboratory of Precision Spectroscopy, East China Normal University, Shanghai, China, ²Collaborative Innovation Center of Extreme Optics, Shanxi University, Taiyuan, China, ³Chongqing Key Laboratory of Precision Optics, Chongqing Institute of East China Normal University, Chongqing, China, ⁴Shanghai Research Center for Quantum Sciences, Shanghai, China

We present an experimental demonstration of an optically controllable phononic low-pass filter in a multimode optomechanical system. By coupling two spatially separated nanomechanical resonators via optomechanical interactions, the phononic signal below a cutoff frequency can be transferred between mechanical resonators, while the signal above the cutoff frequency is attenuated, which resembles an electronic low-pass filter. Moreover, the cutoff frequency is controllable by tuning the optomechanical interaction via the intracavity field. Our results provide an essential element in phononic circuits and have potential applications for information processing in hybrid quantum systems.

Keywords: cavity optomechanics, phononic device, multimode optomechanical system, silicon nitride membrane, phonon filter

1 INTRODUCTION

Phonons, the carriers of heat or acoustic excitations, have attracted tremendous attention and become an emerging research field recently [1]. In contrast to photons and electrons, phonons are usually considered as a waste of energy and detrimental to information processing due to their relatively short lifetime and incoherence. Owing to recent progresses of optomechanics and micro/nano fabrication, not only the lifetime of phonon has been pushed to an unprecedented level [2–5], but also the coherent manipulation of single quanta of sound has been realized [6–9]. Combined with the successes of strong interactions with other types of particles [10–14], and phonon reservoir engineering [15–18], these achievements together make phonons as a promising candidate for classical and quantum information processing. Various phononic devices, such as phononic diodes [19–22], logic gates [23], memories [24–27], and waveguides [28–31], have been developed in the past few decades.

A phononic filter or mechanical filter, which is an essential ingredient for phononic circuits, has been utilized for signal processing since the 1940s [32]. Different approaches and systems have been used to realize phononic filters, for example, liquid helium [33], superlattices [34], coupled mechanical resonators [35–37], and phononic crystals [38–40]. In spite of extensive studies of phononic filters in various systems, most of them are based on purely mechanical or electromechanical devices, the phononic filter with the photon-phonon interface is less investigated, which could play an important role for information processing in future hybrid quantum networks.

In this work, we present a proof-of-principle demonstration of a phononic low-pass filter in a two-membrane-in-the-middle optomechanical system [41–43]. Such a phononic low-pass filter is based on two spatially separated nanomechanical membranes, which are coupled through radiation pressure induced interaction. By sending the mechanical vibration as the input signal upon one membrane and detecting the output signal on the other, we observe that the phononic signal below a cutoff frequency can be transferred, while the signal above the cutoff frequency is attenuated, similar

OPEN ACCESS

Edited by:

Liu Yang,

Harbin Engineering University, China

Reviewed by:

Yan Zhang,

Northeast Normal University, China

Zhi-Cheng Shi,

Fuzhou University, China

*Correspondence:

Jiteng Sheng

jtsheng@ps.ecnu.edu.cn

Specialty section:

This article was submitted to Optics and Photonics, a section of the journal Frontiers in Physics

Received: 25 March 2022

Accepted: 19 April 2022

Published: 04 May 2022

Citation:

Yang C, Sheng J and Wu H (2022) Controllable Phononic Low-Pass Filter via Optomechanical Interactions. *Front. Phys.* 10:904467. doi: 10.3389/fphy.2022.904467

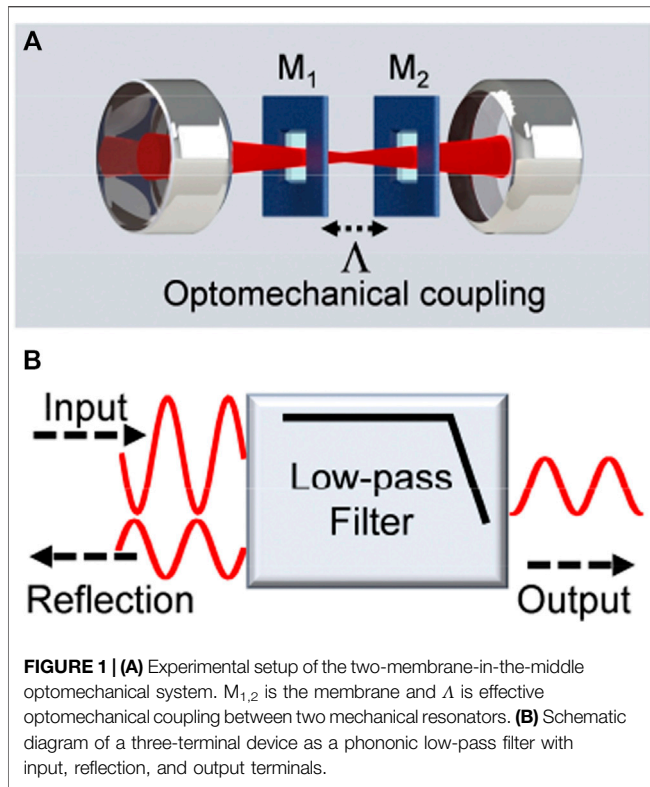


FIGURE 1 | (A) Experimental setup of the two-membrane-in-the-middle optomechanical system. $M_{1,2}$ is the membrane and Λ is effective optomechanical coupling between two mechanical resonators. **(B)** Schematic diagram of a three-terminal device as a phononic low-pass filter with input, reflection, and output terminals.

to an electronic low-pass filter. The phase shift is also measured at different frequencies. By analyzing the response function of such a phononic low-pass filter, we find that it depends on the optomechanical coupling strength, therefore, the cutoff frequency of the low-pass filter can be simply tuned by changing the optical intensity.

The remainder of this paper is organized as follows. In **Section 2**, we describe the experimental setup for the realization of the phononic low-pass filter in the two-membrane-in-the-middle optomechanical system. In **Section 3**, the theoretical model of the two-membrane-in-the-middle system and the basic principle of such a phononic low-pass filter are presented. In **Section 4**, we show the experimental results. **Section 5** serves as the conclusion.

2 EXPERIMENTAL SETUP

The phononic low-pass filter is realized in a two-membrane-in-the-middle optomechanical system, as shown in **Figure 1A**. Two flexible stoichiometric silicon nitride (SiN) membranes are placed inside an optical Fabry-Perot cavity separately with a distance of ~ 60 mm. The membranes have a thickness of 50 nm and a 1×1 mm² size. The vibrational (1, 1) modes are utilized in the experiment, and the mechanical frequencies can be tuned to be degenerate with the piezos [44]. The optical cavity consists of two identical mirrors with a cavity length of 140 mm and a finesse $\sim 1,000$. The cavity is driven by a red-detuned laser field, which interacts with both membranes simultaneously due to the dynamical backaction. Consequently, two individual

membranes are effectively coupled by the cavity field, which provides a channel for transferring phononic information between two membranes. The motions of membranes are monitored by two weak probe laser fields separately.

The experimental setup is similar to the one used to study the phonon heat transport and coupled-mode heat engine [45, 46]. The difference is that a coherent signal is used, instead of the thermal noise. More specifically, the signal with amplitude modulation (AM) is applied as the input signal upon one nanomechanical membrane through the piezo. The dynamics of two membranes are recorded in real-time by a two-channel lock-in amplifier, as the output and reflection signals, respectively. The schematic diagram of such a phononic low-pass filter is shown in **Figure 1B**.

3 THEORETICAL MODEL

The total Hamiltonian of such a two-membrane-in-the-middle optomechanical system in the rotating frame of the driving laser frequency can be written as ($\hbar = 1$) [45].

$$\hat{H} = -\Delta \hat{a}^\dagger \hat{a} + \omega_0 \hat{b}_1^\dagger \hat{b}_1 + \omega_0 \hat{b}_2^\dagger \hat{b}_2 - g_0 \hat{a}^\dagger \hat{a} (\hat{b}_1^\dagger + \hat{b}_1) - g_0 \hat{a}^\dagger \hat{a} (\hat{b}_2^\dagger + \hat{b}_2) + i\varepsilon (\hat{a}^\dagger - \hat{a}) \quad (1)$$

Here \hat{a} and $\hat{b}_{1,2}$ are the annihilation operators of the cavity mode and the mechanical oscillators, respectively. $\Delta = \omega_L - \omega_C$ is the frequency detuning between the driving laser and the cavity resonance. The two degenerate mechanical modes have the same frequency ω_0 . g_0 is the optomechanical coupling strength. $\varepsilon = \sqrt{P\kappa_{in}}/\hbar\omega_L$ is the driving strength, P is the input laser power, and κ_{in} is the loss of the input cavity mirror.

When the damping rate of the cavity mode is much larger than the mechanical damping rates, i.e., $\kappa \gg \gamma_{1,2}$, the cavity field follows the dynamics of the mechanical modes adiabatically, and can be eliminated according to Ref. [45]. Consequently, the system can be described by an effective Hamiltonian

$$\hat{H}_{eff} = \sum_{i=1,2} (\omega_0 + \Lambda - i\gamma_i/2) \hat{b}_i^\dagger \hat{b}_i + \Lambda (\hat{b}_1^\dagger \hat{b}_2 + \hat{b}_2^\dagger \hat{b}_1) \quad (2)$$

Here $\Lambda = g_0^2 \chi_{eff}$ is the effective coupling strength between two membranes, and

$$\chi_{eff} = \frac{P\kappa_{in}/\hbar\omega_L}{\kappa^2/4 + \Delta^2} \left(\frac{\Delta + \omega_0}{\kappa^2/4 + (\Delta + \omega_0)^2} + \frac{\Delta - \omega_0}{\kappa^2/4 + (\Delta - \omega_0)^2} \right) \quad (3)$$

is the effective susceptibility introduced by the intracavity field [45–47]. According to **Eq. 2**, the coupled-mode equations of two mechanical resonators can be obtained as follows

$$\ddot{x}_1 + \gamma_1 \dot{x}_1 + \omega_0^2 x_1 + 2\Lambda \omega_0 (x_2 + x_1) = F_d/m \quad (4)$$

$$\ddot{x}_2 + \gamma_2 \dot{x}_2 + \omega_0^2 x_2 + 2\Lambda \omega_0 (x_1 + x_2) = 0 \quad (5)$$

Here, $x_{1,2} = \sqrt{\frac{\hbar}{2m\omega_0}} (\hat{b}_{1,2}^\dagger + \hat{b}_{1,2})$ is the mechanical displacement, m is the effective mass of membrane, and $F_d = F_0 (1 + M \cos \omega_m t) \cos \omega_0 t$ is the driving force upon the first mechanical resonator with a modulation frequency ω_m and

modulation depth M . The displacements $x_{1,2}$ can be decomposed into $x_{1,2} = X_{1,2}e^{-i\omega_0 t} + X_{1,2}^*e^{i\omega_0 t}$. Consequently, Eqs 4, 5 become

$$\dot{X}_1 + \frac{\gamma_1}{2}X_1 + i\Lambda X_1 + i\Lambda X_2 = \frac{iF_0}{4\omega_0 m} (1 + M \cos \omega_m t) \quad (6)$$

$$\dot{X}_2 + \frac{\gamma_2}{2}X_2 + i\Lambda X_2 + i\Lambda X_1 = 0 \quad (7)$$

Eqs 6, 7 can be expressed in the frequency domain

$$\chi_1^{-1}(\omega)X_1[\omega] + i\Lambda X_2[\omega] = \frac{iF_0}{4\omega_0 m} \quad (8)$$

$$\left(\delta(\omega) + \frac{M}{2}\delta(\omega - \omega_m) + \frac{M}{2}\delta(\omega + \omega_m) \right)$$

$$\chi_2^{-1}(\omega)X_2[\omega] = -i\Lambda X_1[\omega] \quad (9)$$

Here, $\chi_{1,2}(\omega) = [\gamma_{1,2}/2 + i(\Lambda - \omega)]^{-1}$ is the susceptibility function of mechanical resonator. By performing the inverse Fourier transform $f(t) = \int_{-\infty}^{+\infty} F[\omega]e^{-i\omega t}d\omega$, we can obtain $X_1(t)$ and $X_2(t)$ in the time domain as follows

$$X_1(t) = \frac{iF_0}{4\omega_0 m} \left[\chi_{1eff}(0) + \chi_{1eff}(-\omega_m)\frac{M}{2}e^{-i\omega_m t} + \chi_{1eff}(\omega_m)\frac{M}{2}e^{i\omega_m t} \right] \quad (10)$$

$$X_2(t) = \frac{\Lambda F_0}{4\omega_0 m} \left(\chi_2(0)\chi_{1eff}(0) + \chi_2(-\omega_m)\chi_{1eff}(-\omega_m)\frac{M}{2}e^{-i\omega_m t} + \chi_2(\omega_m)\chi_{1eff}(\omega_m)\frac{M}{2}e^{i\omega_m t} \right) \quad (11)$$

with $\chi_{1eff}(\omega) = [\chi_1^{-1}(\omega) + \Lambda^2\chi_2(\omega)]^{-1}$. Thus, $X_1(t)$ and $X_2(t)$ represent the reflection and output (see Figure 1B), respectively. We can also obtain $X_1(t)$ at $\Lambda = 0$ as the input, which is denoted as $X_{10}(t)$. Therefore, the response function can be defined as the ratio between the output and reflection, or the output and input, which are respectively represented by

$$R_1(\omega_m) = \frac{X_2^*[0]X_2[-\omega_m] + X_2[0]X_2^*[\omega_m]}{X_1^*[0]X_1[-\omega_m] + X_1[0]X_1^*[\omega_m]} = \Lambda^2 \frac{\chi_2^*(0)\chi_2(-\omega_m)\chi_{1eff}^*(0)\chi_{1eff}(-\omega_m) + \chi_2(0)\chi_2(\omega_m)\chi_{1eff}(0)\chi_{1eff}^*(\omega_m)}{\chi_{1eff}^*(0)\chi_{1eff}(-\omega_m) + \chi_{1eff}(0)\chi_{1eff}^*(\omega_m)} \quad (12)$$

and

$$R_2(\omega_m) = \frac{X_2^*[0]X_2[-\omega_m] + X_2[0]X_2^*[\omega_m]}{X_{10}^*[0]X_{10}[-\omega_m] + X_{10}[0]X_{10}^*[\omega_m]} = \frac{\gamma_1}{4} (\gamma_1/2 + i\omega_m)\Lambda^2 \left[\chi_2^*(0)\chi_2(-\omega_m)\chi_{1eff}^*(0)\chi_{1eff}(-\omega_m) + \chi_2(0)\chi_2(\omega_m)\chi_{1eff}(0)\chi_{1eff}^*(\omega_m) \right] \quad (13)$$

Please note that $R_1(\omega_m)$ and $R_2(\omega_m)$ only contain the frequency components at ω_m . The DC and high-order harmonics are ignored in order to be consistent with the experimental results. The reason why two response functions are used is that R_1 is defined to be consistent with the experimental measurements and R_2 is the typical definition for

a low-pass filter in electric circuits. As one will see that these two response functions have similar behaviors and only slightly different in the magnitude and the phase shift.

The magnitude ($10\text{Log}|R_{1,2}|$) and phase shift ($\arg [R_{1,2}]$) of the response function as a function of the modulation frequency in the weak coupling regime are plotted in Figure 2. As one can see in Figure 2, the magnitude has a flat response at a relatively small frequency, and has high attenuation above a specific frequency. By analogy to the electronic low-pass filter, we define the frequency at which the transition occurs, i.e. the cutoff frequency, as the magnitude is reduced by 3dB compared to the DC response. The cutoff frequency is marked in Figures 2A,C, which is ~ 10 Hz. Similar to the electronic low-pass filter, a phase shift also exists for such a phononic low-pass filter, which indicates the output signal phase lags behind the reflection or input signal. As one can see in Figures 2B,D, the phase shift is -60 at the cutoff frequency. Compared to the typical passive low-pass filter in electric circuits, the attenuation of such a phononic filter at low frequencies is relatively large. This is due to the relatively large reflection, which means the energy of the input signal partly remains in membrane 1 rather than completely transferring to membrane 2. This situation can be circumvented by introducing mechanical gain and breaking Lorentz reciprocity [20].

When the coupling strength Λ is relatively large, and beyond the critical point, i.e., $\Lambda^2 - (\gamma_1 - \gamma_2)^2/16 = 0$, the system enters into the strong coupling regime, where the normal modes become nondegenerate with the eigenfrequencies $\omega_+ = \omega_0$ and $\omega_- = \omega_0 + 2\Lambda$ [45]. Figure 3 illustrates the response function as a function of ω_m in the strong coupling regime. In contrast to the weak coupling, the magnitude increases gradually as ω_m becomes larger, and reaches a maximum value at $\omega_m = 2|\Lambda|$. As ω_m is further enhanced, the magnitude decreases, as shown in Figures 3A,C. Although the magnitude doesn't have a flat response at low frequencies as the weak coupling case does, we can still define a cutoff frequency similar to the weak coupling case. The reason why there is a peak in the magnitude of the response function is due to the fact that the mechanical power spectrum splits, i.e., the normal mode splitting, in the strong coupling regime [46]. This means that the mechanical susceptibility is modified to be two peaks instead of a single peak in the weak coupling regime. The peaks shown in Figures 3A,C correspond to the situation when sidebands induced by AM are in resonance with the normal modes. In contrast to the weak coupling case, the phase shift at the cutoff frequency is -140 , as shown in Figures 3B,D.

4 EXPERIMENTAL RESULTS

The displacements of membranes $x_{1,2}$ can be decomposed into $x_{1,2}(t) = X_{1,2}^{lock}(t) \cos \omega_o t - Y_{1,2}^{lock}(t) \sin \omega_o t$, where $X_{1,2}^{lock}$ and $Y_{1,2}^{lock}$ are the quadrature components of the lock-in amplifier, and the reference frequency is tuned to be resonant with the mechanical frequency. Figure 4 shows the amplitude of the measured signal, i.e. $\sqrt{(X_{1,2}^{lock})^2 + (Y_{1,2}^{lock})^2}$, as a function of time at different ω_m . The

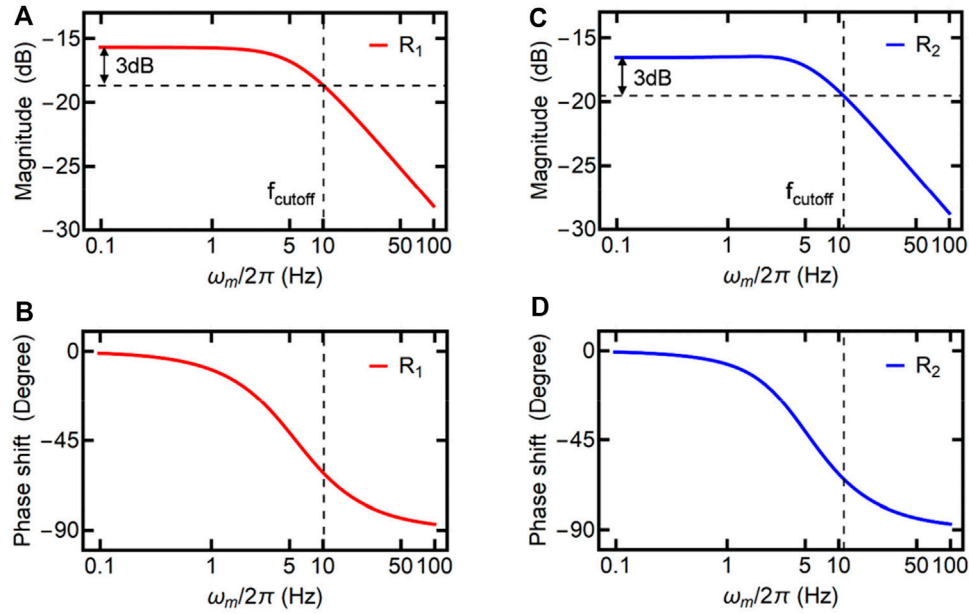


FIGURE 2 | (A) The magnitude and (B) the phase shift of the response function R_1 as a function of ω_m . (C) The magnitude and (D) the phase shift of the response function R_2 as a function of ω_m . The dashed lines are used to indicate the cutoff frequency. The parameters for the theoretical simulations are $\Lambda = -2\pi \times 1$ Hz, $\gamma_1 = 2\pi \times 6$ Hz, and $\gamma_2 = 2\pi \times 12$ Hz.

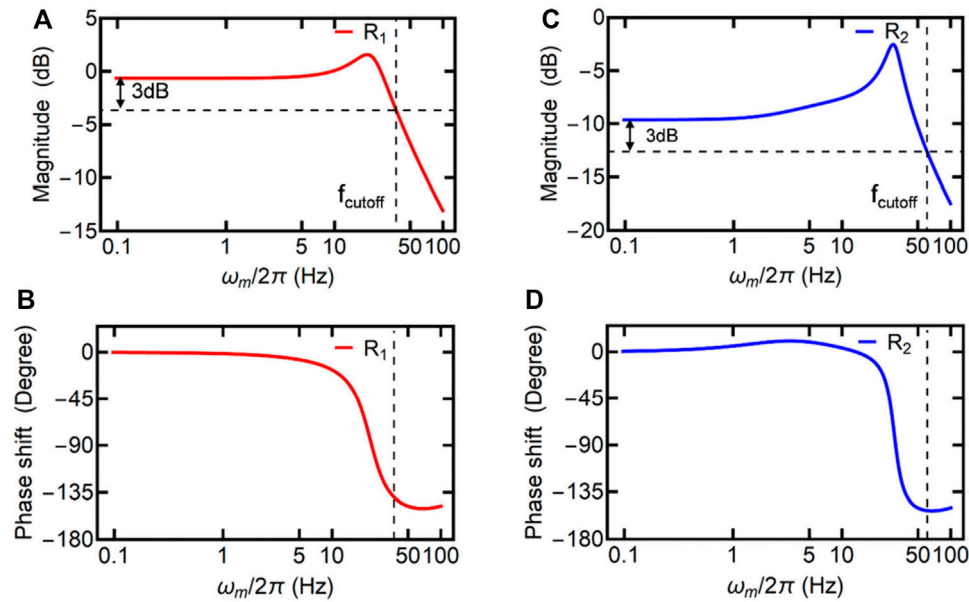
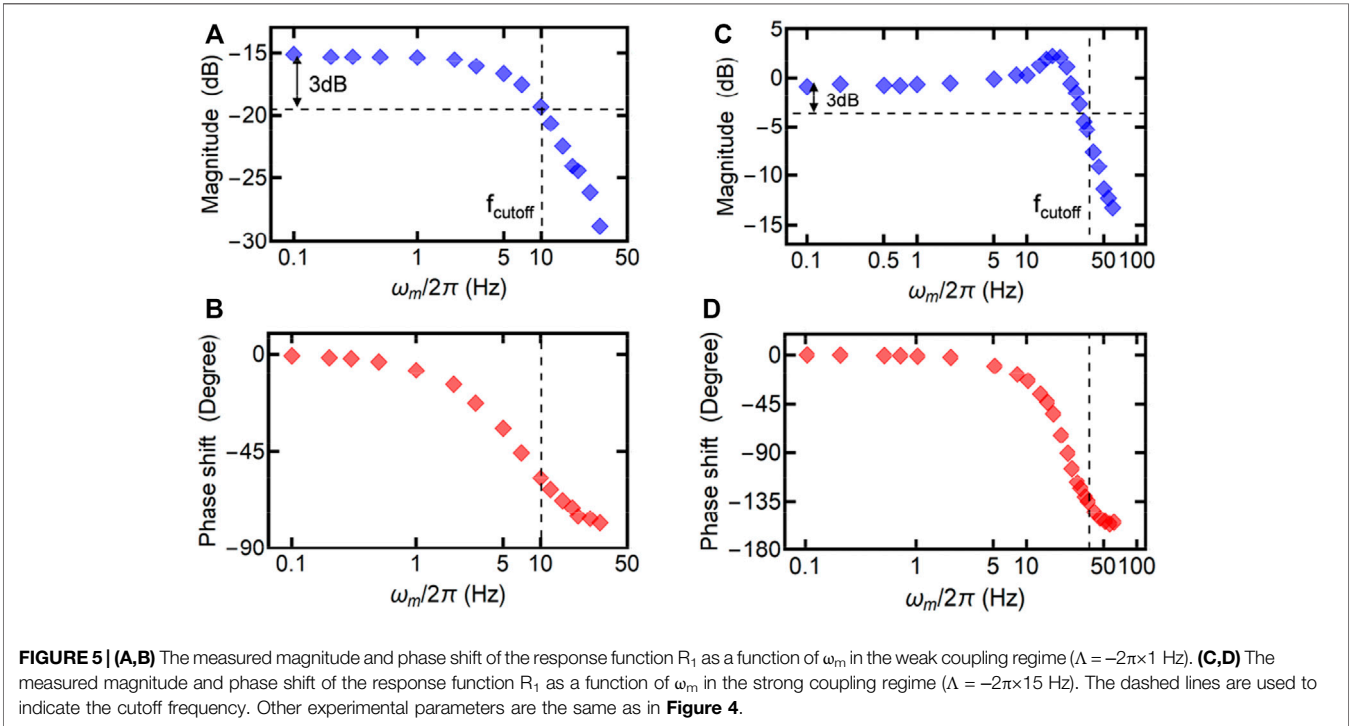
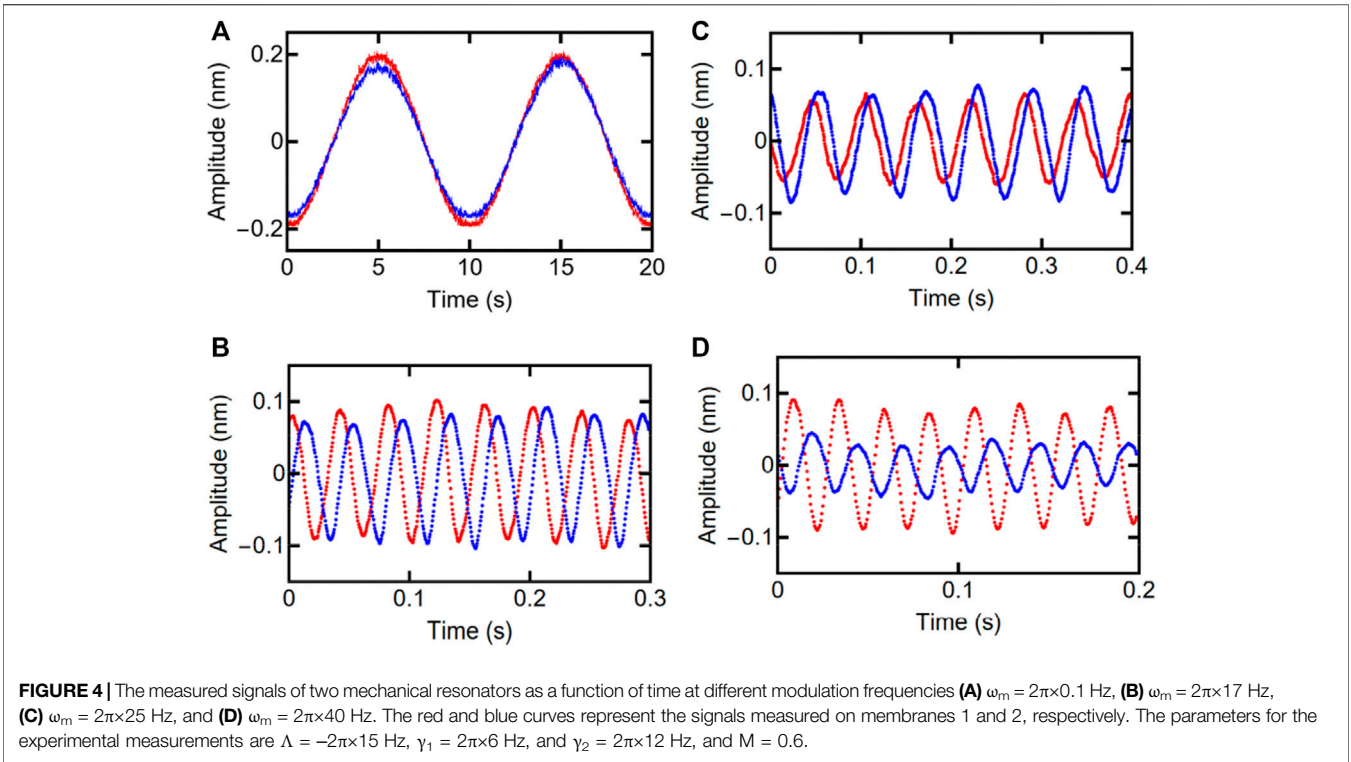


FIGURE 3 | (A) The magnitude and (B) the phase shift of the response function R_1 as a function of ω_m . (C) The magnitude and (D) the phase shift of the response function R_2 as a function of ω_m . The dashed lines are used to indicate the cutoff frequency. The parameters for the theoretical simulations are $\Lambda = -2\pi \times 15$ Hz, $\gamma_1 = 2\pi \times 6$ Hz, and $\gamma_2 = 2\pi \times 12$ Hz.

red and blue curves represent the signals measured on membranes 1 and 2, respectively. As one can see in **Figure 4**, the shift lag between two mechanical resonators becomes larger as ω_m increases. The phase shift in **Figures 4A–D** are -0.5° , -55° ,

-105° , and -145° , respectively. In addition, the amplitude is reduced at a relatively high ω_m . It is worth mentioning that the modulation frequency ω_m is what we are interested in rather than ω_0 , which is the carrier frequency.



By extracting the amplitude and phase information of both membranes at different ω_m , we can plot the measured magnitude and phase shift of the response function R_1 as a function of ω_m . **Figures 5A,B** illustrate the experimental

measurements for the weak coupling regime ($\Lambda = -2\pi \times 1$ Hz), and **Figures 5C,D** are for the strong coupling regime ($\Lambda = -2\pi \times 15$ Hz). The experimental measurements agree with the theoretical simulations very well (see **Figures**

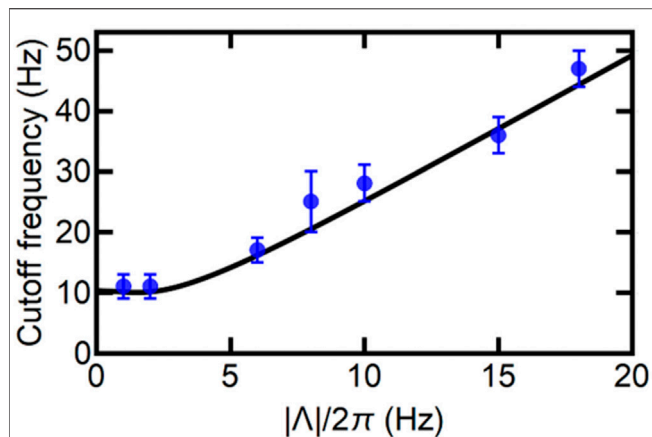


FIGURE 6 | The cutoff frequency as a function of optomechanical coupling strength magnitude $|\Lambda|$. The blue dots are the experimental measurements and the black curve is the theoretical simulation. The error bars are the standard deviations. Other experimental parameters are the same as in **Figure 4**.

2, 3). In both cases, the response is attenuated rapidly above a critical frequency, accompanying with a phase shift. The difference is that the magnitude has a flat response at small frequencies in the weak coupling regime, while the magnitude has a peak response in the strong coupling regime. Moreover, the cutoff frequency is enhanced in the strong coupling regime compared to the weak coupling regime.

Figure 6 presents the cutoff frequency derived from R_1 as a function of $|\Lambda|$. The blue dots are the experimental data and the black curve is the theoretical calculation. According to **Figure 6**, the cutoff frequency can be widely tuned by changing $|\Lambda|$, which can be realized by simply modifying the input laser power. The cutoff frequency approaches a constant (~ 10 Hz) when $|\Lambda|$ is close to zero, and increases linearly at a large $|\Lambda|$. Although the cutoff frequency demonstrated in this work is in the range of Hz, the method is universal and the cutoff frequency can be extended to a much higher frequency by using mechanical resonators with frequencies at gigahertz [11].

REFERENCES

- Li N, Ren J, Wang L, Zhang G, Hänggi P, Li B. Colloquium: Phononics: Manipulating Heat Flow with Electronic Analogs and beyond. *Rev. Mod. Phys.* (2012) 84:1045–66. doi:10.1103/revmodphys.84.1045
- Ghadimi AH, Fedorov SA, Engelsen NJ, Bereyhi MJ, Schilling R, Wilson DJ, et al. Elastic Strain Engineering for Ultralow Mechanical Dissipation. *Science* (2018) 360:764–8. doi:10.1126/science.aar6939
- Tsaturyan Y, Barg A, Polzik ES, Schliesser A. Ultracoherent Nanomechanical Resonators via Soft Clamping and Dissipation Dilution. *Nat Nanotech* (2017) 12:776–83. doi:10.1038/nnano.2017.101
- Norte RA, Moura JP, Gröblacher S. Mechanical Resonators for Quantum Optomechanics Experiments at Room Temperature. *Phys. Rev. Lett.* (2016) 116:147202. doi:10.1103/physrevlett.116.147202
- Reinhardt C, Müller T, Bourassa A, Sankey JC. Ultralow-Noise SiN Trampoline Resonators for Sensing and Optomechanics. *Phys. Rev. X* (2016) 6:021001. doi:10.1103/physrevx.6.021001
- O'Connell AD, Hofheinz M, Ansmann M, Bialczak RC, Lenander M, Lucero E, et al. Quantum Ground State and Single-Phonon Control of a Mechanical Resonator. *Nature* (2010) 464:697. doi:10.1038/nature08967
- Hong S, Riedinger R, Marinković I, Wallucks A, Hofer SG, Norte RA, et al. Hanbury Brown and Twiss Interferometry of Single Phonons from an Optomechanical Resonator. *Science* (2017) 358:203–6. doi:10.1126/science.aan7939
- Kotler S, Peterson GA, Shojaei E, Lecocq F, Cicak K, Kwiatkowski A, et al. Direct Observation of Deterministic Macroscopic Entanglement. *Science* (2021) 372:622–5. doi:10.1126/science.abf2998
- Mercier de Lépinay L, Ockeloen-Korppi CF, Woolley MJ, Sillanpää MA. Quantum Mechanics-free Subsystem with Mechanical Oscillators. *Science* (2021) 372:625. doi:10.1126/science.abf5389
- Chu Y, Kharel P, Renninger WH, Burkhardt LD, Frunzio L, Rakich PT, et al. Quantum Acoustics with Superconducting Qubits. *Science* (2017) 358:199–202. doi:10.1126/science.aao1511
- Gustafsson MV, Aref T, Kockum AF, Ekström MK, Johansson G, Delsing P. Propagating Phonons Coupled to an Artificial Atom. *Science* (2014) 346:207–11. doi:10.1126/science.1257219

5 CONCLUSION

A phononic filter is an important component in the phononic circuits for information processing. We have demonstrated a controllable phononic low-pass filter with cavity optomechanics. The phononic low-pass filter consists of two flexible nanomechanical membranes. The signal applied on one mechanical resonance can be transported to the other over a long distance through light by utilizing cavity-mediated optomechanical interactions. Meanwhile, such a transportation of signal shows a characteristic response function, which is analogous to the low-pass filter in electric circuits. The studies of phononic filters in cavity optomechanical systems could lead to useful tools for classical and quantum information processing.

DATA AVAILABILITY STATEMENT

The original contributions presented in the study are included in the article/Supplementary Material, further inquiries can be directed to the corresponding author.

AUTHOR CONTRIBUTIONS

CY, JS, and HW carried out the experiment, analyzed the data, developed the theory, and wrote the paper.

FUNDING

This research was supported by the National Key R&D Program of China (No. 2017YFA0304201), NSFC (Nos. 11925401, 11734008, 11974115, and 11621404), the Shanghai Municipal Science and Technology Major Project (No. 2019SHZDZX01), Natural Science Foundation of Shanghai (No. 22ZR1420400), Natural Science Foundation Project of CQ (No. cstc2021jcyj-msxmX0914).

12. Mirhosseini M, Sipahigil A, Kalaei M, Painter O. Superconducting Qubit to Optical Photon Transduction. *Nature* (2020) 588:599–603. doi:10.1038/s41586-020-3038-6
13. Arrangoiz-Arriola P, Alex Wollack E, Pechal M, Witmer JD, Hill JT, Safavi-Naeini AH. Coupling a Superconducting Quantum Circuit to a Phononic Crystal Defect Cavity. *Phys. Rev. X* (2018) 8:031007. doi:10.1103/physrevx.8.031007
14. Sheng J, Chao Y, Shaffer JP. Strong Coupling of Rydberg Atoms and Surface Phonon Polaritons on Piezoelectric Superlattices. *Phys. Rev. Lett.* (2016) 117:103201. doi:10.1103/physrevlett.117.103201
15. Metelmann A, Clerk AA. Nonreciprocal Photon Transmission and Amplification via Reservoir Engineering. *Phys. Rev. X* (2015) 5:021025. doi:10.1103/physrevx.5.021025
16. Tomadin A, Diehl S, Lukin MD, Rabl P, Zoller P. Reservoir Engineering and Dynamical Phase Transitions in Optomechanical Arrays. *Phys. Rev. A* (2012) 86:033821. doi:10.1103/physreva.86.033821
17. Otterstrom NT, Behunin RO, Kittlaus EA, Rakich PT. Optomechanical Cooling in a Continuous System. *Phys. Rev. X* (2018) 8:041034. doi:10.1103/physrevx.8.041034
18. Naseem MT, Müstecaplıoğlu ÖE. Ground-state Cooling of Mechanical Resonators by Quantum Reservoir Engineering. *Commun. Phys.* (2021) 4:95. doi:10.1038/s42005-021-00599-z
19. Li B, Wang L, Casati G. Thermal Diode: Rectification of Heat Flux. *Phys. Rev. Lett.* (2004) 93:184301. doi:10.1103/physrevlett.93.184301
20. Zhang J, Peng B, Özdemir ŞK, Liu Y-x., Jing H, Lü X-y., et al. Giant Nonlinearity via Breaking Parity-Time Symmetry: A Route to Low-Threshold Phonon Diodes. *Phys. Rev. B* (2015) 92:115407. doi:10.1103/physrevb.92.115407
21. Kalantar N, Agarwalla BK, Segal D. Harmonic Chains and the Thermal Diode Effect. *Phys. Rev. E* (2021) 103:052130. doi:10.1103/PhysRevE.103.052130
22. Kargı C, Naseem MT, Opatrný T, Müstecaplıoğlu ÖE, Kurizki G. Quantum Optical Two-Atom Thermal Diode. *Phys. Rev. E* (2019) 99:042121. doi:10.1103/PhysRevE.99.042121
23. Wang L, Li B. Thermal Logic Gates: Computation with Phonons. *Phys. Rev. Lett.* (2007) 99:177208. doi:10.1103/physrevlett.99.177208
24. Wang L, Li B. Thermal Memory: A Storage of Phononic Information. *Phys. Rev. Lett.* (2008) 101:267203. doi:10.1103/physrevlett.101.267203
25. Bagheri M, Poot M, Li M, Pernice WPH, Tang HX. Dynamic Manipulation of Nanomechanical Resonators in the High-Amplitude Regime and Non-volatile Mechanical Memory Operation. *Nat Nanotech* (2011) 6:726–32. doi:10.1038/nano.2011.180
26. Merklein M, Stiller B, Vu K, Madden SJ, Eggleton BJ. A Chip-Integrated Coherent Photonic-Phononic Memory. *Nat Commun* (2017) 8:574. doi:10.1038/s41467-017-00717-y
27. Sheng J, Wei X, Yang C, Wu H. Self-Organized Synchronization of Phonon Lasers. *Phys. Rev. Lett.* (2020) 124:053604. doi:10.1103/PhysRevLett.124.053604
28. Fu W, Shen Z, Xu Y, Zou C-L, Cheng R, Han X, et al. Phononic Integrated Circuitry and Spin-Orbit Interaction of Phonons. *Nat Commun* (2019) 10:2743. doi:10.1038/s41467-019-10852-3
29. Taylor JC, Kindel WF, Chatterjee E, Kindel WF, Soh D, Eichenfield M. Reconfigurable Quantum Phononic Circuits via Piezo-Acoustomechanical Interactions. *npj Quantum Inf* (2022) 8:19. doi:10.1038/s41534-022-00526-2
30. Hatanaka D, Mahboob I, Onomitsu K, Yamaguchi H. Phonon Waveguides for Electromechanical Circuits. *Nat Nanotech* (2014) 9:520–4. doi:10.1038/nano.2014.107
31. Safavi-Naeini AH, Painter O. Design of Optomechanical Cavities and Waveguides on a Simultaneous Bandgap Phononic-Photonic Crystal Slab. *Opt. Express* (2010) 18:14926. doi:10.1364/oe.18.014926
32. Adler R. Compact Electromechanical Filters, *Electronics* (1947) 20, 100–105.
33. Wyatt AFG, Lockerbie NA, Sherlock RA. LiquidHe4: A Tunable High-Pass Phonon Filter. *Phys. Rev. Lett.* (1974) 33:1425–8. doi:10.1103/physrevlett.33.1425
34. Narayanamurti V, Störmer HL, Chin MA, Gossard AC, Wiegmann W. Selective Transmission of High-Frequency Phonons by a Superlattice: The "Dielectric" Phonon Filter. *Phys. Rev. Lett.* (1979) 43:2012–6. doi:10.1103/physrevlett.43.2012
35. Lin L, Howe RT, Pisano AP. Microelectromechanical Filters for Signal Processing. *J. Microelectromech. Syst.* (1998) 7:286–94. doi:10.1109/84.709645
36. Hajhashemi MS, Amini A, Bahreyni B. A Micromechanical Bandpass Filter with Adjustable Bandwidth and Bidirectional Control of Centre Frequency. *Sensors Actuators A Phys* (2012) 187:10–5. doi:10.1016/j.sna.2012.08.008
37. Ilyas S, Chappanda KN, Younis MI. Exploiting Nonlinearities of Micro-machined Resonators for Filtering Applications. *Appl. Phys. Lett.* (2017) 110:253508. doi:10.1063/1.4986921
38. D'Alessandro L, Belloni E, Ardito R, Braghin F, Corigliano A. Mechanical Low-Frequency Filter via Modes Separation in 3D Periodic Structures. *Appl. Phys. Lett.* (2017) 111:231902. doi:10.1063/1.4995554
39. Dong Y, Yao H, Du J, Zhao J, Ding C. Research on Bandgap Property of a Novel Small Size Multi-Band Phononic Crystal. *Phys Lett A* (2019) 383:283–8. doi:10.1016/j.physleta.2018.10.042
40. Chen Z-G, Zhao J, Mei J, Wu Y. Acoustic Frequency Filter Based on Anisotropic Topological Phononic Crystals. *Sci Rep* (2017) 7:15005. doi:10.1038/s41598-017-15409-2
41. Piergentili P, Catalini L, Bawaj M, Zippilli S, Malossi N, Natali R, et al. Two-membrane Cavity Optomechanics. *New J. Phys.* (2018) 20:083024. doi:10.1088/1367-2630/aad85f
42. Gärtner C, Moura JP, Haaxman W, Norte RA, Gröblacher S. Integrated Optomechanical Arrays of Two High Reflectivity SiN Membranes. *Nano Lett.* (2018) 18:7171–5. doi:10.1021/acs.nanolett.8b03240
43. Wei X, Sheng J, Yang C, Wu Y, Wu H. Controllable Two-Membrane-In-The-Middle Cavity Optomechanical System. *Phys. Rev. A* (2019) 99:023851. doi:10.1103/physreva.99.023851
44. Wu S, Sheng J, Zhang X, Wu Y, Wu H. Parametric Excitation of a SiN Membrane via Piezoelectricity. *AIP Adv* (2018) 8:015209. doi:10.1063/1.5009952
45. Yang C, Wei X, Sheng J, Wu H. Phonon Heat Transport in Cavity-Mediated Optomechanical Nanoresonators. *Nat Commun* (2020) 11:4656. doi:10.1038/s41467-020-18426-4
46. Sheng J, Yang C, Wu H. Realization of a Coupled-Mode Heat Engine with Cavity-Mediated Nanoresonators. *Sci Adv* (2021) 7:eabl7740. doi:10.1126/sciadv.abl7740
47. Xu H, Mason D, Jiang L, Harris JGE. Topological Energy Transfer in an Optomechanical System with Exceptional Points. *Nature* (2016) 537:80–3. doi:10.1038/nature18604

Conflict of Interest: The authors declare that the research was conducted in the absence of any commercial or financial relationships that could be construed as a potential conflict of interest.

Publisher's Note: All claims expressed in this article are solely those of the authors and do not necessarily represent those of their affiliated organizations, or those of the publisher, the editors and the reviewers. Any product that may be evaluated in this article, or claim that may be made by its manufacturer, is not guaranteed or endorsed by the publisher.

Copyright © 2022 Yang, Sheng and Wu. This is an open-access article distributed under the terms of the Creative Commons Attribution License (CC BY). The use, distribution or reproduction in other forums is permitted, provided the original author(s) and the copyright owner(s) are credited and that the original publication in this journal is cited, in accordance with accepted academic practice. No use, distribution or reproduction is permitted which does not comply with these terms.